Temperature-Dependent Recombination Dynamics of Photocarriers in $CsPbBr_3$ Microcrystals Revealed by Ultrafast Terahertz Spectroscopy

Sheng Lee[1], Kyeongdeuk Moon[2], Muhammad Shoaib[2], Charles N. B. Pedorella[3], Kellen O'Brien[3], Meng-Ju Sher[3], Seokhyoung Kim[2], Tyler L. Cocker[1,]*

[1]Department of Physics and Astronomy, Michigan State University, East Lansing, MI 48824, USA
[2]Department of Chemistry, Michigan State University, East Lansing, MI 48824, USA
[3]Department of Physics, Wesleyan University, Middletown, CT 06459, USA
*cockerty@msu.edu

Abstract

We study the ultrafast dynamics of photoexcited charge carriers in micron-scale crystals composed of the inorganic perovskite $CsPbBr_3$ with time-resolved terahertz spectroscopy. Exciting with photon energy close to the band edge, we find that a fast (< 10 ps) decay emerges in the terahertz photoconductivity with increasing pump fluence and decreasing temperature, dominating the dynamics at 4 K. The fluence-dependent dynamics can be globally fit by a nonlinear recombination model, which reveals that the influence of different nonlinear recombination mechanisms in the studied pump fluence range depends on temperature. Whereas the Auger scattering rate decreases with decreasing temperature from 77 K to 4 K, the radiative recombination rate increases by three orders of magnitude. Spectroscopically, the terahertz photoconductivity resembles a Drude response at all delays, yet an additional Lorentz component due to an above-bandwidth resonance is needed to fully reproduce the data.

Introduction

The dynamics of carrier recombination and hot-carrier cooling in halide perovskites are important considerations for improving solar energy and light emission devices based on these materials. For example, for a single-junction solar cell, the Shockley-Queisser limit establishes a maximum energy conversion efficiency of ~30% [1], assuming photogenerated charge carriers cool to the band edge of the absorbing material (with a band gap of 1.1 eV) before being extracted. Whereas multi-junction solar cells exceed this limit by incorporating many absorbing materials with different band gaps [2], another strategy is to extract the carriers before they cool to the band edge [3]. The corresponding device is known as a hot-carrier solar cell and has a maximum energy conversion efficiency of 66% (under one sun illumination) for a single-junction cell [4]. Halide perovskites have emerged as a promising absorber for next-generation solar cells thanks to their ease of processing [5], low cost [6], efficient absorption [7], and outstanding carrier transport properties [8,9], with solar cells based on perovskite compounds reaching energy conversion efficiencies >25% [10]. The discovery of slow hot-carrier cooling in halide perovskites [11–16] has opened additional avenues, including the possibility of perovskite-based hot-carrier solar cells [3,17,18].

The key to realizing a hot-carrier solar cell is to engineer a device in which carrier cooling to the band edge is slower than the carrier extraction process. This is a significant obstacle due to the typical relaxation timescales of semiconductors following photoexcitation: (i) the nonequilibrium carrier population first reaches a Boltzmann distribution at elevated temperature (i.e., with energy well above the conduction band minimum) on the 10-fs timescale via carrier-carrier scattering; (ii) the carrier temperature subsequently decreases via scattering with optical phonons, cooling to the lattice temperature on the 100-fs timescale [19]. The dynamics can be even faster in organic materials used for solar cells [20,21]. In halide perovskites, however, including mixed organic-inorganic compounds, the carrier cooling time can be extended, with the specific mechanism impacting the dynamics determined by the photoexcited carrier density [17]. At high carrier density (~10^{18} cm^{-3}), the slow decay of optical phonons into acoustic phonons leads to a saturation of the optical phonon population and, consequently, a suppression of carrier cooling through optical phonon emission [22]. This effect is known as the hot-phonon bottleneck and has been observed in lead-halide perovskites [12–16], leading to fluence-dependent carrier cooling times that reach the picosecond timescale [17]. Auger recombination also plays an important role in perovskite dynamics for carrier densities of ~10^{18} cm^{-3} by enhancing electron-hole recombination on the sub-10-ps timescale while simultaneously creating a hot-carrier population [16]. Meanwhile, at lower carrier densities ($<10^{18}$ cm^{-3}), the formation of large polarons slows carrier cooling [17,23,24]. Thus, the photoexcited carrier density is a critical parameter for understanding the evolution of hot carriers in perovskites. The dynamics of the photoexcited carrier population is similarly critical. Mobile charge carriers may decay via trapping into defect sites (a 1-particle process), direct electron-hole recombination (2-particle process), or Auger recombination (3-particle process). Of these processes, only electron-hole recombination produces photoluminescence, which is useful for light-emitting devices. Conversely, although the Auger process results in an electron and hole recombining, the third charge carrier receives the excess energy, and thus may be extracted as a hot carrier with potentially high efficiency in a solar energy device. Therefore, unravelling the importance of each recombination mechanism in a given scenario (i.e., at different temperatures, fluences, etc.) is of paramount importance for optimizing different types of devices based on halide perovskites.

Ultrafast terahertz (THz) spectroscopy has been employed to study charge carrier dynamics in both hybrid organic-inorganic [24–32] and all-inorganic [32-35] halide perovskites. In the pump-probe modality known as time-resolved THz spectroscopy (TRTS), an optical pump pulse photoexcites the sample and the THz photoconductivity (i.e., the transient complex conductivity at THz frequencies) is measured with sub-picosecond temporal resolution by a time-delayed, single-cycle THz probe pulse. TRTS applied to thin films of $CH_3NH_3PbI_3$ has revealed fluence-dependent recombination dynamics following photoexcitation with pump fluences in the 1 – 100 μJ/cm^2 range. These dynamics changed with decreasing temperature, with Auger recombination highly dependent on a structural phase transition [27]. In single-crystal $CH_3NH_3PbI_3$, ultrabroadband TRTS has been used to simultaneously track the coherent motion of charge carriers and the correlated motion of the polar lattice, thereby resolving polaron formation on the timescale of the longitudinal optical phonon period following band-edge excitation [24]. Other ultrafast experimental schemes using THz pulses have also been employed, including a pump-push-probe approach to study carrier cooling [36], THz emission spectroscopy to study coherent vibrational dynamics [37], and nonlinear THz spectroscopy to control the perovskite lattice [38]. Most recently, a saturation of the THz photoconductivity at optical-pump/THz-probe delays greater than

10 ps was identified for increasing optical pump fluence in halide perovskite ($CsPbBr_3$, CH_3NH_3 and γ-$CsPbI_3$) films at temperatures down to 77 K. This effect was attributed to the formation of a stable Mott polaron density in the $10^{17} – 10^{18}$ cm^{-3} range [32], which decreases with decreasing temperature. It was proposed that a stable Mott polaron density explains the relatively strong Auger recombination in these materials [32].

Here, we explore micrometer-scale single crystals of $CsPbBr_3$ with TRTS as a function of temperature, extending the range of study down to liquid helium temperatures. By examining structures larger than the quantum or mesoscopic confinement regimes, we exclude structural effects on the conductivity and dynamics. Meanwhile, the high crystalline quality of the microcrystals minimizes defect-related effects that may dominate the dynamics of thin films. The absence of a structural phase transition in $CsPbBr_3$ between room temperature and 4 K [39,40] further simplifies the comparison of dynamics at different temperatures. We excite the samples with pump photon energies close to the band edge and find that a <10 ps decay emerges in the THz photoconductivity with increasing pump fluence and decreasing temperature, dominating the dynamics at 4 K. The complex photoconductivity is best described at all temperatures and delay times by a Drude-Lorentz model, where the Drude and Lorentz contributions correspond to photoexcited free charge carriers and the tail of an above-bandwidth resonance, respectively. The decay of the THz photoconductivity is primarily determined by the dynamics of the free charge carrier population. At a given temperature (77 K or 4 K), the fluence-dependent decays may be globally fit by a nonlinear recombination model with universal rate parameters. These rate parameters reveal the mechanism that dominates the fast decay in our samples at each temperature for 515 nm pump fluence in the range of 1.8 – 16.6 μJ/cm^2 (corresponding to carrier densities in the range of $10^{16} – 10^{18}$ cm^{-3}). Whereas the Auger recombination rate is slightly lower at 4 K than at 77 K, direct electron-hole recombination is at least three orders of magnitude larger at 4 K than at 77 K, and thus becomes the dominant nonlinear recombination mechanism at 4 K for carrier densities less than 10^{18} cm^{-3}.

Results and discussion

Figure 1 illustrates the general concept of a TRTS experiment on a semiconducting sample for high optical pump fluences (for $CsPbBr_3$, carrier densities in the $10^{17} – 10^{18}$ cm^{-3} range). Employing an optical pump pulse with photon energy close to the band gap, photoexcitation promotes electrons into the conduction band near the conduction band minimum, leaving holes in the valence band near its maximum, as shown in Fig. 1A. The right side of Fig. 1A represents this situation schematically in terms of the density of photoexcited free carriers, n, which are measured by a THz probe pulse. Photoexcited electrons and holes may recombine, but scattering (e.g., with phonons) restricts this process because an electron-hole pair must have approximately zero net momentum to recombine radiatively. Thus, temperature may affect the decay dynamics of photoexcited carriers through the phonon population. When n is sufficiently large (as defined by the Auger scattering cross section) efficient electron-hole recombination can proceed via a three-particle process. Specifically, an electron and hole recombine while donating their excess energy

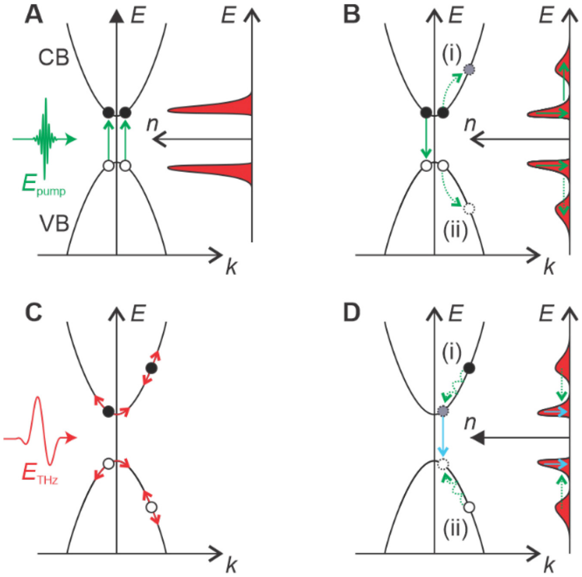

Figure 1*. *Probing ultrafast high-density carrier dynamics with THz pulses. *(A) An ultrafast optical pump pulse, E_{pump}, with energy (2.4 eV) near the direct band gap of $CsPbBr_3$ excites (green arrows) free charge carriers, i.e., electrons (black-filled circles) in the conduction band (CB) and holes (white-filled circles) in the valence band (VB). Right: schematic representation of photoexcited free charge carrier density, n. (B) At high carrier densities, Auger recombination plays a prominent role in the evolution of the free charge carrier density. Left: an electron and hole may recombine and give the resulting energy to a third particle – either an electron (i) or a hole (ii) – rather than emitting a photon. Right: the charge carrier density near the band edges decreases during the Auger process (solid green arrows) while simultaneously generating secondary hot charge carrier peaks in the CB and/or VB (dashed green arrows). (C) A time-delayed THz pulse, E_{THz}, probes the intraband conductivity of all photoexcited free charge carriers,*

both at the band extrema and at elevated points in the band structure. (D) Hot electrons (i) and hot holes (ii) cool to the band edges via many optical phonon scattering events (green dashed lines, not to scale) before ultimately recombining (solid cyan arrow). Right: carrier cooling to the lattice temperature shifts the hot carrier peaks towards the band extrema (dashed green arrows), while ongoing electron-hole recombination at the band edge continues to decrease the primary peaks at the band edges.

and momentum to the third particle (either an electron or a hole), thereby promoting it to an elevated state in the band structure. Two examples are shown in Fig. 1B: (i) an electron is excited within the conduction band or (ii) a hole is excited within the valence band. Only one valance and conduction band are shown in the schematic, but an electron (hole) may also be excited to a higher-lying conduction band (lower-lying valence band). Therefore, Auger recombination not only reduces the photoexcited carrier density near the band extrema, but also creates secondary carrier density peaks at elevated carrier temperature (i.e., at higher energy; Fig. 1B, right). In the case of $CsPbBr_3$, this corresponds to carriers with 2.3 eV of excess energy (which is the energy of a 540 nm photon from the suppressed PL process). Incidentally, this is almost equal to the initial pump photon energy of 2.4 eV in our experiments.

In a TRTS experiment, the THz pulse arrives after the pump excitation and probes the intraband conductivity of the photoexcited electrons and holes. Unlike the optical pulse, the THz pulse does not move the carriers to a new band (since its center photon energy is only ~4 meV) but rather "sloshes" the carriers within the band, as shown in Fig. 1C. Higher mobility carriers, such as those with lower scattering rate and lower effective mass, absorb the THz probe field more effectively. Hence, carriers that are heated beyond the parabolic region of the band extrema or into satellite valleys, where the effective mass is larger, have less influence on the THz field [41,42]. Nevertheless, they are still probed by the THz pulse, so the THz photoconductivity is in principle sensitive to both carriers at the band extrema and those at elevated temperatures. Hot carriers typically cool to the band extrema via optical phonon scattering before recombining, as shown in Fig. 1D.

The TRTS experimental geometry for this study is illustrated in Fig. 2A. An ultrafast optical pump pulse (515 nm wavelength, 230 fs pulse duration) excites the sample, which is comprised of

CsPbBr$_3$ microcrystals on an M-cut sapphire substrate. A THz probe pulse is transmitted through the sample at a delay time t_p after optical photoexcitation and detected coherently by electro-optic sampling. The M-cut sapphire substrate was rotated to orient the THz polarization along the fast axis of the substrate, thereby avoiding artifacts related to substrate birefringence. The pump polarization was oriented parallel to the THz polarization.

An optical PL image (see Optical Characterization for further details) of a typical region of the sample is shown in Fig. 2B. Rectangular-shaped microcrystals with edge lengths on the 10-μm length scale are observed across the sample surface. The in-plane alignment of the microcrystals is not universal, i.e., the orientation of the nominally rectangular-shaped microcrystals varies across the substrate. The uniformity of the microcrystals apparent in PL images suggests most are either single crystals or composed of no more than two to three 10-μm-scale crystallites (see, e.g.,

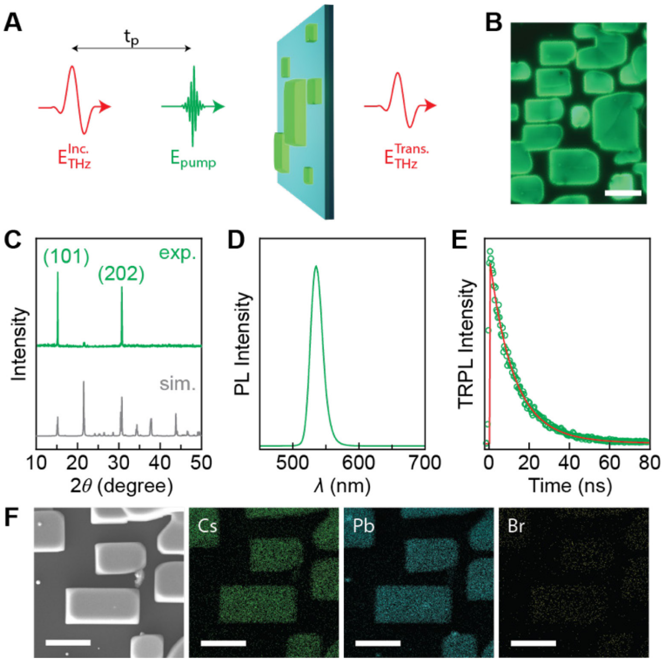

Figure 2*. *CsPbBr$_3$ microcrystals characterization. *(A) Schematic illustration of measurement geometry. (B) Optical PL image of the CsPbBr$_3$ microcrystals; scale bar, 10 μm. (C) Experimental (top) and simulated (bottom) XRD patterns of orthorhombic CsPbBr$_3$. (D-E) PL spectrum (D) and time-resolved PL decay spectrum of CsPbBr3 microcrystals. (F) SEM image and elemental distribution maps; all scale bars, 5 μm.*

large crystals containing faint dark lines in Fig. 2B). The crystalline quality of the sample is further supported by powder XRD measurements and simulations (Fig. 2C).

Figure 2D shows an example PL spectrum for the sample, with an emission peak near 540 nm; the corresponding absorption, for comparison, is reported in reference [43]. Complementary time-resolved photoluminescence measurements are shown in Fig. 1E. The data in both Fig. 2D and Fig. 2E correspond to spatial averages over many microcrystals, not the response of a single microcrystal. Similarly, the TRTS measurements average over the 1-mm-diameter focal spot of the probing THz pulse (and the sample is mounted on a metallic 1-mm-

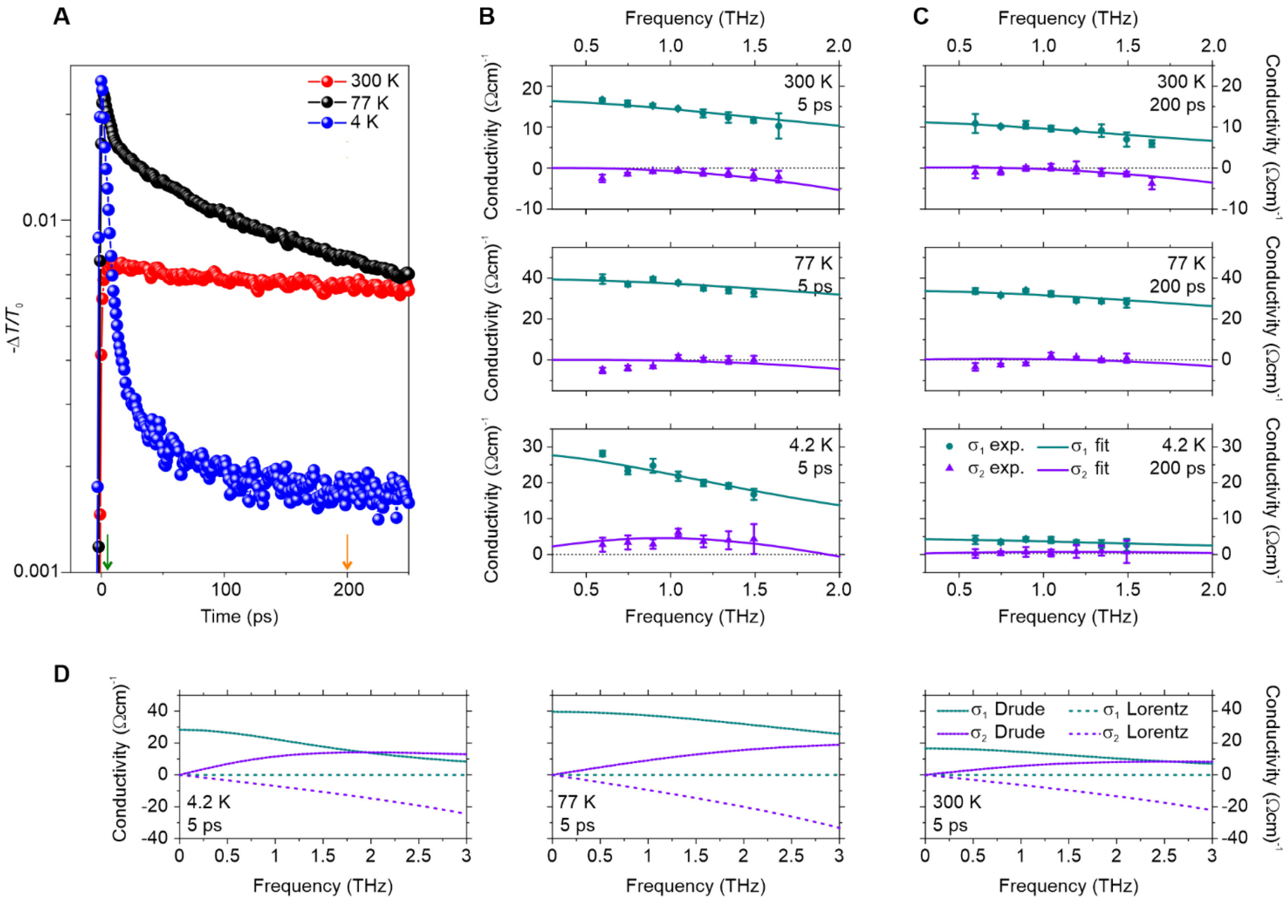

__Figure 3__. __Time-resolved terahertz spectroscopy of CsPbBr$_3$ microcrystals__. (A) Optical-pump / terahertz-probe dynamics following photoexcitation by a 515 nm (230 fs long) pump pulse. Circles: relative change to the peak of the transmitted terahertz field. (B,C) Time-resolved terahertz spectroscopy 5 ps (B) and 200 ps (C) following optical excitation, at 4.2 K, 77 K, and 300 K

(bottom to top). Dark cyan circles: real part of the experimental complex conductivity, σ_1*; purple triangles: imaginary part of the experimental complex conductivity,* σ_2*; dark cyan lines: fits to experimental* σ_1 *based on a Drude + Lorentz model (see text); purple lines: simultaneous fits to experimental* σ_2 *based on a Drude + Lorentz model. (D) Contributions of the Drude component (*σ_1*: short-dashed dark cyan curves;* σ_2*: short-dashed purple curves) and Lorentz component (*σ_1*: long-dashed dark cyan curves;* σ_2*: long-dashed purple curves) to the Drude + Lorentz model fits in (B).*

diameter aperture for ease of alignment and fluence calibration). Finally, an SEM image and (color-coded) elemental map distributions are shown in Fig. 2F, confirming the expected stoichiometry.

The interaction of the THz probe with the sample is detected through changes to the electric-field waveform of the transmitted pulse. Differential changes to the peak field ($-\Delta T/T_0$), specifically, may be associated with the spectrally averaged THz photoconductivity. Figure 3A shows $-\Delta T/T_0$ as a function of pump-probe delay time for three temperatures (300 K, 77 K, 4 K) and the same optical pump fluence of 16.6 μJ/cm^2.

We highlight that the dynamics of $-\Delta T/T_0$ change significantly with temperature. At 300 K, the THz photoconductivity decays exponentially, which appears linear when visualized on a log-linear plot (e.g., Fig. 3A). An exponential fit yields a decay time of 2.5 ns. Decreasing the pump fluence leads to an increasing decay time (not shown). For fluences of 3 μJ/cm^2 and below, the decay time reaches $\geq$ 10 ns, which is the longest decay time that can be reasonably fit for our (full) scan range of 500 ps. This is consistent with the previously reported photoluminescence decay time of 8.7 ns observed in $CsPbBr_3$ single-crystal nanowires synthesized by the same method [43].

Cooling the sample to 77 K, the dynamics change significantly: the charge carriers show an emerging fast, non-exponential decay component within the initial 30 ps following optical excitation. We investigate the fast decay dynamics further by lowering the sample temperature down to liquid helium temperature. At 4 K, the amplitude of the fast decay is dramatically enhanced. It comprises 90% of the decay from the peak photoconductivity to the equilibrium state for a pump fluence of 16.6 μJ/cm^2 at 4 K, whereas it constitutes ~30% of the decay at 77 K for the same pump fluence.

To better understand the dynamics, we perform TRTS at 5 ps (Fig. 3B) and 200 ps (Fig 3C) at all three temperatures for a pump fluence of 16.6 μJ/cm^2. The real (σ_1) and imaginary (σ_2) components of the complex THz photoconductivity were extracted in each case. At all temperatures and delays, the complex THz conductivity exhibits a Drude-like shape; however, a pure Drude model fit is insufficient to quantitatively fit the data. Slightly negative values of σ_2 for some spectra present a particular challenge to Drude model fitting. We considered a number of conventional modifications to the Drude model to capture these observations: (i) Although the morphology of the sample (i.e., separated microcrystals; see Fig. 2B) suggests that effective medium theory (EMT) may be necessary to describe the conductivity, neither Bruggeman nor Maxwell-Garnett EMT provides an improved agreement with the experimental data, indicating the structure size is large enough to neglect depolarization (plasmonic) effects, to first order. (ii) Similarly, the microcrystal sizes are too large to provide weak carrier confinement of the type described by the Drude-Smith model [44-46]. Still, we tested the Drude-Smith model fitting, but found that it did not adequately improve agreement with the experimental data. (iii) σ_1 was not better reproduced by a modified power law corresponding to a large polaron [24]. (iv) Finally, we achieved improved agreement with the experimental data (see Fig. 3B and 3C) by adding a Lorentz term to the Drude model fit, such that the total complex conductivity is given by

$$\tilde{\sigma}(\omega) = \frac{n_{\text{Drude}} e^2 \tau_{\text{Drude}}}{m^*}\left(\frac{1}{1-i\omega\tau_{\text{Drude}}}\right) + \frac{n_{\text{Lorentz}} e^2}{m^*}\left(\frac{\omega}{\omega/\tau_{\text{Lorentz}} + i\left(\omega_0^2-\omega^2\right)}\right) \quad , \tag{1}$$

where n_{Drude} is the photoexcited density of free charge carriers in the Drude model, τ_{Drude} is the scattering time of the free charge carriers, $1/\tau_{\text{Lorentz}}$ is the damping parameter of a resonator with frequency $f_0 = \omega_0/2\pi$, e is the elementary charge, m^* is the charge-carrier effective mass, and n_{Lorentz} parameterizes the spectral weight of the Lorentz oscillator, as is discussed further below. We find that the resonance peak is well above the spectral bandwidth of our probe pulses, such that the Lorentz component has minimal effect on σ_1. However, it contributes significantly to σ_2, as shown in Fig. 3D. This below-resonance Lorentzian conductivity is largely insensitive to the damping parameter of the resonator, but scales linearly with n_{Lorentz}. A similar fit to the conductivity may be obtained by keeping the ratio n_{Lorentz}/f_0^2 constant, provided $f_0 > 2.5$ THz.

Parameter degeneracy can be addressed in the Drude-Lorentz fitting procedure by fixing some of the parameters in Equation (1) using known physical values. However, this necessitates a physical interpretation of the Lorentz oscillator. Two possibilities are described below:

(I) The Lorentzian conductivity may be attributed to the polarizability of photoexcited excitons in the material. Exciton binding energies of ~40 meV have been reported in the literature [39, 47 - 53], which is consistent with the strong photoluminescence in our samples at room temperature (Fig. 2) and the spacing we observe between the PL peak (Fig. 2D) and absorption onset (reference [43]) at room temperature. We note that an Elliott fit to low-temperature absorption data would be a useful further point of comparison [54] but was not available for this study. In THz spectroscopy, the primary signature of excitons is a Lorentz resonance at their 1*s*-2*p* intra-excitonic transition frequency [30,55,56], i.e., 7.5 THz. Setting f_0 = 7.5 THz and assuming the effective mass to be $m^* = m_e \approx m_h \approx 0.2 \times 9.11*10^{-31}$kg [57] for all delay times and temperatures, Drude-Lorentz fits to the experimental data may be obtained using three free parameters: n_{Drude}, n_{Lorentz}, and τ_{Drude}, as shown in Fig. 3B and 3C. Table 1 summarizes the extracted fit parameters; uncertainties were determined through an automated fitting procedure.

Temperature (K)	n_{Drude}(5ps) (10^{18} cm^{-3})	n_{Lorentz}(5ps) (10^{18} cm^{-3})	τ_{Drude}(5ps) (fs)	n_{Drude}(200ps) (10^{18} cm^{-3})	n_{Lorentz}(200ps) (10^{18} cm^{-3})	τ_{Drude}(200ps) (fs)
4	0.25±0.02	1.7±0.2	82±8	0.045±0.007	0.20±0.07	68±14
77	0.72±0.25	2.3±0.8	39±15	0.56±0.15	2.0±0.6	43±13
300	0.19±0.02	1.6±0.2	62±10	0.12±0.01	1.1±0.1	67±10

Table 1: Carrier density parameters for Drude + Lorentz fits to the complex THz conductivities in Fig. 3B and Fig. 3C.

Associating n_{Lorentz} with the transient density of excitons following photoexcitation allows us to compare our Drude-Lorentz fitting results with the absorbed pump photon density. For a fluence of 16.6 μJ/cm^2 and penetration depth of 100 nm [58], the absorbed photon density is 4.3×10^{18} cm^{-3}. Table 1 shows that not only is n_{Lorentz} below this value for all fits, as expected, but also that the majority of photoexcited charge carriers are created as excitons. This potentially explains the surprisingly low photon-to-free-carrier branching ratio observed here and in a previous study [32].

Although it is challenging to definitively associate the Lorentzian conductivity with excitons, there is precedent in the literature. For example, a TRTS study of $CH_3NH_3PbI_3$ has reported intra-excitonic Rydberg transitions and an exciton binding energy of 13.5 meV below 160 K [30]; our results indicate that similar resonances may be expected for ultrabroadband TRTS of $CsPbBr_3$ microcrystals, as the oscillator in our Drude-Lorentz model would be the lowest of these Rydberg transitions. Meanwhile, recent studies of quasi-two-dimensional lead-halide perovskites – which have exciton binding energies greater than 200 meV due to reduced dielectric screening – have combined TRTS with optical spectroscopy to quantify charge carrier and exciton populations as a function of pump-probe delay, fluence, temperature, and pump wavelength [59-61]. Notably, Burgos-Caminal *et al*. also fit their ultrabroadband THz photoconductivities with a Drude-Lorentz model [59]. The Lorentz oscillator peak in their study was well above the measurement bandwidth and was attributed to the polarizability of excitons, as in the present case, which allowed them to extract the exciton and free charge carrier densities. In references [59-61], the measured ratios of free charge carriers to excitons were compared to the temperature-dependent predictions of the Saha equation. Surprisingly, the low-temperature density of free charge carriers in quasi-two-dimensional perovskites significantly exceeds the Saha equation predictions. This is consistent with our observations, summarized in Table 1, where ratios at 4 K of 15±2% and 23±9% were found at 5 ps and 200 ps, respectively, compared to a vanishingly small ratio predicted by the Saha equation. A potential reason for this difference is discussed later.

Although it has previously been observed that the Saha equation fails to accurately predict free charge carrier densities in perovskites with large exciton binding energies at low temperature, the general trend predicted by the Saha equation of decreasing charge carrier density relative to exciton density with decreasing temperature is still expected. In Table 1, the fit parameters at 4 K and 77 K follow this trend, but the parameters at 300 K do not. This may be due to a lower absorbed photon density at 300 K. As can be seen in Fig. 2A, the initial photoconductivity is lower at 300 K than at the other two temperatures despite identical excitation conditions. This likely stems from a longer pump penetration depth at 300 K than at 4 K or 77 K, as a redshift of the absorption onset is expected with decreasing temperature [58].

(II) A possible alternate explanation for the Lorentz oscillator arises due to the strong electron-phonon coupling in lead-halide perovskites. In transmission-mode THz spectroscopy studies of $CsPbBr_3$ nanocrystals, it has been reported that a phonon mode observed in the absence of photoexcitation may be enhanced by optical photoexcitation [33-35]. To the best of our knowledge, signatures of this type have not been reported in larger single crystals to date. However, they have been observed in $CsPbBr_3$ colloidal nanocrystals [33,34] and $CsPbBr_3$ nanocrystal thin films [35] (though at different frequencies in the two cases), as well as in $CH_3NH_3PbI_3$ [25], $CH_3NH_3PbI_{3-x}Cl_x$ [26], and $CH_3NH_3PbI_3(Cl)$ [29] thin films. The photoconductivity is typically fit with a Drude-Lorentz (or Drude-Smith-Lorentz) model in these studies [26,29,33,34]. We therefore performed THz time-domain spectroscopy of our $CsPbBr_3$ microcrystal samples to determine whether the Lorentz oscillator component in our measured photoconductivities is also present in the absence of photoexcitation, but the results were inconclusive due to substrate thickness variations.

The mechanism leading to the photo-enhancement of phonon resonances in TRTS of lead-halide perovskites merits further discussion, since this is not typically observed in conventional semiconductors, as has been noted elsewhere [35]. In ultrabroadband THz spectroscopy performed in reflection mode, Lan *et al*. have demonstrated that photoexcited charge carriers in $CH_3NH_3PbI_3$ single crystals form polarons by coupling to a single effective longitudinal optical phonon at 3.7 THz, which is a mixture of a Pb-I stretch mode and a translational and vibrational motion of the CH_3NH_3 cation [24]. The key observation in these experiments was coherent beating along the pump-probe time axis that changed phase at a probe frequency matching the effective phonon frequency, rather than an enhanced phonon mode in spectroscopy. Conversely, the photo-enhanced resonances in transmission-mode TRTS of thin films of $CH_3NH_3PbI_3$ and similar compounds have been observed near 1 and 2 THz [26,27,29]. It is also worth noting that transmission-mode THz time-domain spectroscopy of the unexcited sample is sensitive to transverse optical modes rather than longitudinal optical modes [60].

Meanwhile, Cinquanta *et al*. have attributed three Lorentzian peaks between 0.5 THz and 2.0 THz in transmission-mode TRTS of $CsPbBr_3$ nanocrystal thin films to phonon modes enhanced by polaronic coupling through comparison with density functional theory calculations [35]. Similar (ultrabroadband) experiments on $CsPbBr_3$ colloidal nanocrystal solutions have observed weaker peaks near 2 THz and 3 THz [33,34]. The size and shape of small nanocrystals may also affect which modes participate in the coupling, and how strongly. Thus, although electron-phonon coupling and polaronic effects are important considerations for lead-halide perovskites, the variation of photo-enhanced Lorentzian peaks across samples and the relative sparsity of analogous signatures in transmission-mode TRTS of single-crystal samples makes direct comparison to our results challenging. Nevertheless, we note that many TRTS studies of lead-halide perovskites have been performed with a bandwidth of ~ 0.5 – 2 THz, as in this study, and hence above-bandwidth resonances may have escaped attention.

At all temperatures, the shape (i.e., curvature) of the THz complex conductivity in our experiments exhibits minimal changes between 5 ps and 200 ps, so the dynamics of the sample are captured almost entirely by the decay of n_{Drude} and n_{Lorentz} in our model. (In interpretation II, the fits are the same, but $n_{\mathrm{Lorentz}}e^2/m^*$ would be replaced by a generic oscillator strength parameter.). The similarity of the conductivity at 5 ps and 200 ps further indicates that we do not observe a shift of spectral weight from n_{Drude} to n_{Lorentz} that would signify exciton formation between 5 ps and 200 ps. Moreover, inspection of the THz electric-field waveforms (not shown) reveals that the decay of $-\Delta T/T_0$ is primarily due to a decrease in the transmitted field peak (correlated with σ_1) rather than a shift of the peak (correlated with σ_2). Since σ_1 is dominated by the Drude component in our spectral bandwidth, $-\Delta T/T_0$ is approximately proportional to n_{Drude}, though the similarity of our spectroscopy results at 5 ps and 200 ps implies n_{Lorentz} decays at the same rate. We note that time-dependent changes to the effective mass may slightly modify the $-\Delta T/T_0$ dynamics [32], but we expect this effect to be minimal in our experiments due to our near-band-edge pump photon energy.

We explore the dynamics further in fluence-dependent $-\Delta T/T_0$ measurements, as shown in Fig. 4. At 4 K, the fast decay component dominates the dynamics (Fig. 4A). It is present at all pump fluences studied, with an estimated onset of ~1 μJ/cm^2. This stands in contrast to the behavior observed at 77 K, where it only emerges above a fluence threshold >6 μJ/cm^2 and comprises a smaller fraction of the overall decay (Fig. 4B). We model the dynamics via a differential equation that describes the free carrier recombination rate [27],

$$dn_{\mathrm{Drude}}/dt = -k_1 n_{\mathrm{Drude}} - k_2 {n_{\mathrm{Drude}}}^2 - k_3 {n_{\mathrm{Drude}}}^3 \ , \tag{2}$$

where k_1 corresponds to an exponential decay in $n_{\mathrm{Drude}}(t)$, e.g., due to defect trapping, k_2 corresponds to a two-particle decay such as radiative recombination, and k_3 corresponds to a three-particle decay such as Auger recombination. It is worth noting that the similar effective masses of electrons and holes in $CsPbBr_3$ enables this clear distinction, unlike many other semiconductors.

Equation 2 can be solved numerically to yield $n_{\mathrm{Drude}}(t)$ for a given set of coefficients, k_1, k_2, k_3. A nonuniform carrier density profile within the sample complicates this procedure, so the experimental geometry must be carefully considered. The microcrystals studied here have an average thickness of 1 μm, while the absorption depth of the 515 nm pump pulses is estimated to be 100 nm [58], so the absorbed photon density is maximum at the surface and decays exponentially into the material on a length scale shorter than the sample thickness (i.e., the carrier density profile is nonuniform along the thickness of the material). We therefore model $n_{\mathrm{Drude}}(t,z)$ using a series of infinitesimally thin cross sections of carrier density at depth z, each of which has a time dependence governed by Equation (2) (see also, [28]). This procedure is necessary to obtain a reasonable global fit to all $-\Delta T/T_0$ curves at a given temperature using a set of universal fit parameters, k_1, k_2, and k_3. In our model, we assume that the role of diffusion – which acts to spread the initial carrier density profile into the bulk of the sample – is minimal within the relevant time window. We set the initial spatially averaged carrier density, $n_{\mathrm{Drude}}(t = 0)$, using the fixed point determined from TRTS at 5 ps, i.e., $n_{\mathrm{Drude}}(5\text{ ps})$, for a pump fluence of $F = 16.6$ μJ/cm^2. The initial photoexcited carrier density (at $t = 0$) is assumed to scale linearly for other pump fluences. Global fits to the $-\Delta T/T_0$ curves at a given temperature (Fig. 4A, B) thus yield the set of universal parameters shown in Table 2. (For the 77 K data, $k_1 = (1.56 \pm 0.08) \times 10^9$ s^{-1}, while at 4 K, the best fit was obtained with a very small k_1 term, corresponding to a decay too slow to be measured reliably in our experiments.) The resulting set of fluence-dependent carrier decays not only exhibits a fast decay that emerges with increasing fluence, but also predicts a saturating carrier density after the fast decay is complete, consistent with previous experimental observations [32].

Temperature (K)	k_2 (cm^3/s)	k_3 (cm^6/s)
4	$(1.17 \pm 0.06) \times 10^{-6}$	2.6×10^{-26} (upper bound)
77	1.03×10^{-9} (upper bound)	$(8.5 \pm 0.4) \times 10^{-26}$

Table 2: Nonlinear parameters for global fits in Fig. 4A and Fig. 4B.

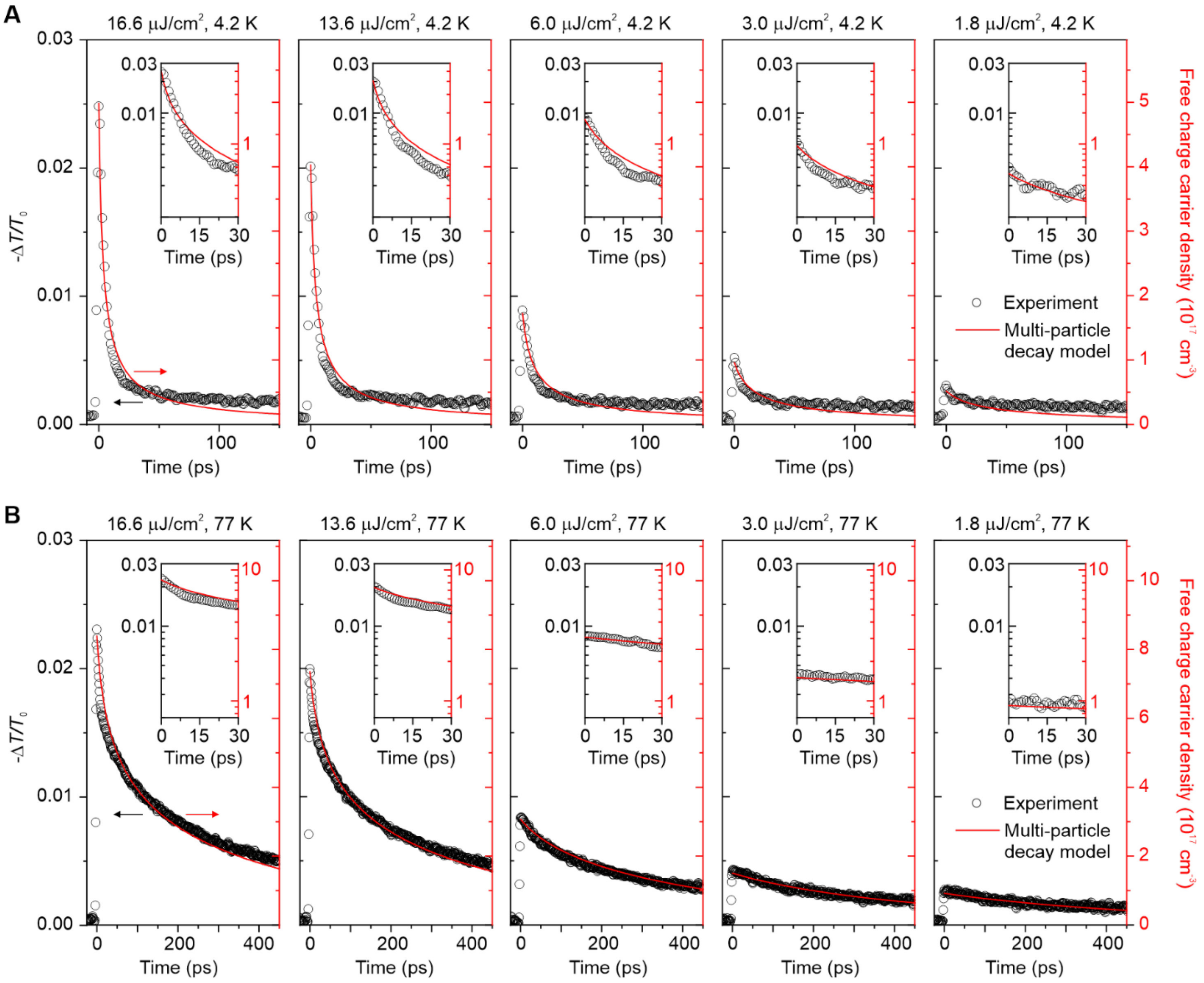

***Figure 4. Ultrafast dynamics revealed by optical-pump / THz-probe experiments** (A) Optical-pump / terahertz-probe dynamics at 4.2 K following photoexcitation by a 515 nm (230 fs long) pump pulse, at a sequence of optical pump fluences (increasing right to left). Hollow black circles: experimental change to the peak of the transmitted terahertz field (-ΔT/T, left axis); solid red lines: global fit to a nonlinear model of charge carrier density decay (right axis). (B) Optical-pump / terahertz-probe dynamics at 77 K at the same pump fluences as in (A). Hollow black circles: experimental data (left axis); solid red lines: fit to a nonlinear model of charge carrier density decay (right axis). The decay parameters at each temperature are fit globally for all fluences. Insets show a magnified view of fits to the fast decay at early times for each panel.*

The parameters k_2 and k_3 define carrier densities above which fast, non-exponential terms contribute significantly to $n_{\text{Drude}}(t)$. Rewriting Equation (2) as$dn_{\text{Drude}}/dt = -(k_1 + k_2 n_{\text{Drude}} + k_3 {n_{\text{Drude}}}^2)n_{\text{Drude}}$, the slope of $n_{\text{Drude}}(t)$ over an infinitesimally short time at t is given by $k_1 + k_2 n_{\text{Drude}} + k_3 {n_{\text{Drude}}}^2$. When n_{Drude} is large, e.g., at early times and high pump fluences, the slope is dominated by the highest order term, but its significance drops off quickly with carrier density (and hence t) due to the nonlinearity. More generally, calculating the slope based on a set of (k_1, k_2, k_3) parameters reveals which term (and hence physical process) contributes most strongly to the instantaneous carrier density decay for a given n_{Drude} and the range of n_{Drude} over which each term is most influential.

Although our global fits used one set of parameters (k_1, k_2, k_3) to fit the data at all fluences for a given temperature, examining the time-dependent rate highlights the relative influence of the various physical processes at different times, fluences, and temperatures. Additionally, we observe a long-lived photoconductivity at 4 K that is not well captured by the nonlinear recombination model (since its magnitude increases along with the non-exponential decay). To most accurately quantify the competition between k_2 and k_3 we therefore prioritize the fit to $-\Delta T/T_0$ at early times over the long tail at later times. Specifically, we fit the slope and fluence-dependence of the slope over the first 30 ps of the decay using k_2 and k_3 (see insets of Fig. 4A,B), with k_1 subsequently used to provide the best overall fit to the full range.

At 4 K, the decay rate, fluence dependence, and fluence onset of the fast dynamics are all best captured by radiative recombination, which is parameterized by a relatively large k_2 term. The fluence onset in Fig. 4A is a particularly clear marker of this dependence, as the fast decays are observable even at the lowest fluences studied. In contrast, at 77 K (Fig. 4B), the fast decay observed at early time disappears for fluences below 13.6 μJ/cm^2. The relatively strong nonlinear fluence onset in this case indicates that the fast decay is dominated by the k_3 term, i.e., by the three-particle Auger recombination process described in the Introduction. Thus, although all three decay processes are in principle always present, the importance of each one in a given scenario may be quantified, with the parameters in Table 2 determining their range of strongest influence. In Table 2, the term “upper bound” indicates that the corresponding parameter cannot be made larger than this value without degrading the quality of the fit; if k_2 or k_3 is an upper bound for a given fit, it means the other term dominates the fast decay. The largest difference between 4 K and 77 K is an increase in k_2 with decreasing temperature, whereas k_3 is roughly constant. This temperature-dependence of k_2 agrees well with the calculations of Davies *et al*. based on the van Roosbroeck-Shockley relation [54].

Meanwhile, the onset carrier density for Auger recombination has important implications for the physics of the material. Previously, Zhang *et al*. fit TRTS data with the Drude-Smith model to define the onset carrier density for fast THz photoconductivity dynamics in $CsPbBr_3$ thin films at 78 K ($\sim 10^{17}$ cm^{-3}) and found that the result coincided with their calculation result for a Mott density of polarons [32]. This approach implies an absorbed-photon-to-charge (branching) ratio below 10%. In contrast, Milot *et al*. and Rehman *et al*. used absorbed photon density to constrain the initial photoinduced carrier density when solving Equation (2) to fit their THz photoconductivity data for $CH_3NH_3PbI_3$ and similar thin films [27,28], noting that a branching ratio near unity is expected [28]. In references [27] and [32], as in our experiments (Fig. 3B and 3C), the imaginary part of the THz complex conductivity is suppressed relative to Drude model predictions. σ_2 also includes negative regions that cannot be reproduced by the Drude model. Whereas the Drude-Smith model can generate negative imaginary conductivities [32], it applies for systems in which charge carriers are structurally confined on the length scale they diffuse during one oscillation of the probing field [46]. Although such confinement may be present in some perovskite thin films, we remove this possibility by studying large microcrystals, and hence may associate deviations from the Drude model with a density of photoexcited excitons (I). It is important to reconsider the concept of a Mott density of polarons within this context. Although the free charge carrier densities from our TRTS measurements and fitting agree roughly with those of Zhang *et al*. [32], the interaction between these carriers and a large background density of excitons would complicate the picture. Recently, interactions between charge carriers and excitons – dubbed Fermi polarons – has been reported for ultrafast two-dimensional optical measurements of monolayer transition metal dichalcogenides [62,63]. A similar scenario merits further investigation in perovskites, especially single crystals.

Finally, the low-temperature dynamics shown in Fig. 4A contains further evidence for the presence of excitons. A long-lived free-carrier population has been observed in quasi-two-dimensional halide perovskites [59,60], similar to the offset in Fig. 4A that is not captured by the solution to

Equation (2). A number of possible mechanisms have been discussed [59-61], but we find the proposal of Burgos-Caminal *et al*. best describes our observations: exciton-exciton annihilation leads to one electron-hole pair recombining and the other breaking apart through an Auger process, thereby providing an ongoing source of free-charge-carriers [59]. This is consistent with the increase of the long-lived photoconductivity in our experiments with increasing pump fluence (and hence exciton density).

Conclusion

Time-resolved THz spectroscopy of $CsPbBr_3$ microcrystals reveals the emergence of a <10 ps, non-exponential decay with increasing optical pump fluence and decreasing temperature. These dynamics can be globally fit by a model incorporating multi-particle decay processes. We find that the radiative recombination rate (k_2) increases by a factor of at least 10^3 with decreasing temperature from 77 K to 4 K, whereas the Auger scattering rate (k_3) decreases slightly over the same temperature range. As a result, the dominant nonlinear recombination mechanism changes from Auger scattering at 77 K to radiative recombination at 4 K for carrier densities in the range of $10^{16} – 10^{18}$ cm^{-3}. The THz complex conductivity at all temperatures and delays tested is well-described by a Drude-Lorentz model. The Drude component of the photoconductivity corresponds to free charge carriers, while we have presented two possible interpretations for the Lorentz oscillator component: (I) a significant density of excitons that contribute primarily to the imaginary part of the THz photoconductivity via the low-frequency tail of the 1*s*-2*p* intra-excitonic transition; (II) an above-bandwidth phonon resonance that is enhanced by strong electron-phonon coupling. Distinguishing these two effects should motivate future low-temperature studies of charge carrier dynamics in highly crystalline lead-halide perovskites.

Methods

$CsPbBr_3$ crystal growth. $CsPbBr_3$ microcrystals were grown on M-plane sapphire (University Wafer) cut in 1 cm × 1 cm size in our home-built CVD system [43]. Growth substrates were cleaned by sequentially sonicating in acetone (Sigma-Aldrich; ACS reagent, ≥ 99.5 %) and iso-propanol (Sigma-Aldrich; ACS reagent, ≥ 99.5 %), blow-dried with nitrogen gas, treated in an ozone cleaner (Samco UV-1) at 150 ℃ for 5 min, and placed 11 cm downstream from the furnace center. $PbBr_2$ (Thermo-Scientific Chemicals; 99.998 % (metals basis)) and CsBr (Thermo-Scientific Chemicals; 99 % (metals basis)) powders were placed in a quartz source boat at the center of a single-zone tube furnace (Fisher Scientific; Lindberg/Blue M Mini-Mite). Prior to the reaction, the quartz tube was baked at 950 ℃ for 1 hour with 50 sccm of Ar gas under vacuum and then was allowed to cool down to the room temperature. After loading substrates and precursors, pressure was raised to 0.13 Torr with a constant 100 sccm Ar flow and temperature was raised at 50 ℃/min ramp rate to 420 ℃. The reaction was allowed to run for 30 minutes. Heating was then stopped and the sample was allowed to cool to 300 ℃ with the furnace closed. The furnace was then opened to an Ar flow until the sample temperature dropped below 250 ℃.

Optical Characterization. Optical images were acquired using a Zeiss upright optical microscope. Dark-field (DF) images were acquired using micro-LED light with a dark filter cube (ZEISS), and photoluminescence (PL) images were taken with a filter cube (BP 450-490 nm for excitation (ZEISS), LP 500 nm for emission (Thorlabs)). Static PL spectra were collected by fiber-coupling PL emission from the microscope to a grating spectrograph (Horiba iHR550) interfaced with liquid-nitrogen-cooled CCD detector (Horiba Symphony II). Time-resolved photoluminescence (TRPL) measurements were performed using a time-correlated single-photon counting (TCSPC) detector with a 405 nm pulsed source (Picoquant, LDH-D-C-405M, CW-80 MHz). The data acquisition card (Edinburgh Instrument, TCC900) and the photomultiplier tube detector (Hamamatsu, H7422-40) were used to record the TRPL.

Structural and elemental analysis. Powder X-ray Diffraction (pXRD) was obtained on Bruker D8 advance diffractometer using Cu Kα radiation (λ = 1.5418 Å). Scanning electron microscope (SEM) images were acquired using a JEOL 7500F with a cold field emission emitter in secondary electron detection mode. The JEOL 7500F was equipped with an Oxford energy-dispersive spectroscopy (EDS) system, which was used for elemental analysis and mapping.

Time-resolved THz spectroscopy measurements. The ultrafast time-resolved THz spectroscopy (TRTS) setup is based on a Carbide laser from Light Conversion operating at 1 MHz repetition rate, which generates near-infrared pulses with 230-fs pulse duration and 1030-nm center frequency. In the home-built THz setup, the THz probe pulses are produced by tilted-pulse-front optical rectification of 10-μJ near-infrared pulses in a lithium niobate crystal (Oxide Corporation). The bandwidth of the pulses available for spectroscopy is approximately 0.5 – 2.0 THz, as confirmed by TRTS of a GaAs test sample. The field of the THz pulses transmitted through the sample is detected by electro-optic sampling in a ZnTe crystal (Del Mar Photonics) using a < 20 fs gate pulse centered at 800 nm. The gate pulse is produced by white-light generation in a YAG crystal using 1030-nm laser pulses and subsequent compression and spectral filtering in a prism compressor. The optical pump pulses used for TRTS are produced by second-harmonic generation in a BBO crystal. The pump pulses have 515 nm center wavelength and approximately 230 fs pulse duration. A maximum pulse energy of 2 μJ is available for pumping the $CsPbBr_3$ sample. The sample was mounted on a 1-mm-diameter aperture and the pump spot diameter was larger than 3 mm to ensure uniform illumination. The highest pump fluence available in our setup is 16.6 uJ/cm^2. Both the optical pump and THz probe pulse trains were modulated during TRTS experiments, such that reference and sample THz waveforms were recorded simultaneously, and each set of waveforms was repeated at least ten times and averaged to minimize drift-related artifacts. Extraction of the complex THz conductivity, $\tilde{\sigma}(\omega) = \sigma_1(\omega) + i\sigma_2(\omega)$, from TRTS measurements followed the standard procedure, using the thin-film formula, and is described in detail elsewhere [64]. The uncertainties for the complex THz conductivity data were determined using the standard deviation of the ten datasets. Evaluation of the sample under a wide-area optical microscope showed the filling factor of the microcrystals to be 0.55; the extracted complex THz conductivity was therefore divided by 0.55 to determine the conductivity within the microcrystals. Pump-probe measurements of the THz-peak transmission change ($-\Delta T/T_0$) were recorded at the modulation frequency of the pump for optimal signal-to-noise ratio and averaged over many scans to minimize drift-related artifacts. Measurements of $-\Delta T/T_0$ were not normalized by the filling factor.

Acknowledgement

The authors thank V. N. Breslin, R. Loloee, R. Bennett, and B. Bi for technical support. T.L.C. acknowledge support from the Cowen Family Endowment. S.K. acknowledges startup support from the Department of Chemistry at Michigan State University. Research at Wesleyan University (M.-J.S., K.O. and C.N.B.P.) is supported by NSF DMR-2316827.

References

[1] W. Shockley. And H. J. Queisser, “Detailed balance limit of efficiency of p-n junction solar cells.” J. Appl. Phys. **32**, 510–519 (1961).

[2] M. Yamaguchi, F. Dimroth, J. F. Geisz, N. J. Ekins-Daukes, “Multi-junction solar cells paving the way for super high-efficiency.” J. Appl. Phys. **129**, 240901 (2021).

[3] S. Kahmann and M. A. Loi, “Hot carrier solar cells and the potential of perovskites for breaking the Shockley–Queisser limit,” J. Mater. Chem. C, **7**, 2471 (2019)

[4] R. T. Ross and A. J. Nozik, “Efficiency of hot-carrier solar energy converters,” J. Appl. Phys. **53**, 3813–3818 (1982).

[5] N. D. Park and K. Zhu, “Scalable fabrication and coating methods for perovskite solar cells and solar modules,” Nat. Rev. Mater. **5**, 333–350 (2020).

[6] T. Brenner, D. Egger, L. Kronik, G. Hodes, and D. Cahen, “Hybrid organic—inorganic perovskites: low-cost semiconductors with intriguing charge-transport properties,” Nat. Rev. Mater. **1**, 15007 (2016).

[7] S. De Wolf, J. Holovsky, S.-J. Moon, P. Loeper, B. Niesen, M. Ledinsky, F.-J. Haug, J.-H. Yum, and C. Ballif, “Organometallic Halide Perovskites: Sharp Optical Absorption Edge and Its Relation to Photovoltaic Performance,” J. Phys. Chem. Lett. **5**, 1035–1039 (2014).

[8] S. D. Stranks, G. E. Eperon, G. Grancini, C. Menelaou, M. J. P. Alcocer, T. Leijtens, L. M. Herz, A. Petrozza, and H. J. Snaith, “Electron–hole diffusion lengths exceeding 1 micrometer in an organometal trihalide perovskite absorber,” Science **342**, 341–344 (2013).

[9] L. M. Herz, “Charge-carrier mobilities in metal halide perovskites: fundamental mechanisms and limits,” ACS Energy Lett. **2**, 1539–1548 (2017).

[10] Best Research-Cell Efficiency Chart. https://www.nrel.gov/pv/cell-efficiency.html.

[11] G. Xing, N. Mathews, S. Sun, S. S. Lim, Y. M. Lam, M. Grätzel, S. Mhaisalkar, T. C. Sum, **“**Long-Range Balanced Electron- and Hole-Transport Lengths in Organic-Inorganic $CH_3NH_3PbI_3$,” Science. **342**, 344–347 (2013).

[12] M. B. Price, J. Butkus, T. C. Jellicoe, A. Sadhanala, A. Briane, J. E. Halpert, K. Broch, J. M. Hodgkiss, R. H. Friend, and F. Deschler, “Hot-carrier cooling and photoinduced

refractive index changes in organic-inorganic lead halide perovskites," Nat. Commun. **6**, 8420 (2015).

[13] Y. Yang, D. Ostrowski, R. France, K. Zhu, J. Lagemaat, J. M. Luther and M. C. Beard, "Observation of a hot-phonon bottleneck in lead-iodide perovskites," Nature Photon **10**, 53–59 (2016).

[14] T. C. Sum, N. Mathews, G. Xing, S. S. Lim, W. K. Chong, D. Giovanni, and H. A. Dewi, "Spectral Features and Charge Dynamics of Lead Halide Perovskites: Origins and Interpretations," Acc. Chem. Res. **49**, 294–302 (2016).

[15] J. Yang, X. Wen, H. Xia, R. Sheng, Q. Ma, J. Kim, P. Tapping, T. Harada, T. W. Kee, F. Huang, Y. Cheng, M. Green, A. Ho-Baillie, S. Huang, S. Shrestha, R. Patterson and G. Conibeer, "Acoustic-optical phonon up-conversion and hot-phonon bottleneck in lead-halide perovskites," Nat. Commun. **8**, 14120 (2017).

[16] J. Fu, Q. Xu, G. Han, B. Wu, C. H. A. Huan, M. L. Leek and T. C. Sum, "Hot carrier cooling mechanisms in halide perovskites," Nat. Commun. **8**, 1300 (2017).

[17] M. Li, J. Fu, Q. Xu and T. C. Sum, "Slow Hot-Carrier Cooling in Halide Perovskites: Prospects for Hot-Carrier Solar Cells," Adv. Mater. **31**, 1802486 (2019).

[18] I. Ahmed, L. Shi, H. Pasanen, P. Vivo, P. Maity, M. Hatamvand and Y. Zhan, "There is plenty of room at the top: generation of hot charge carriers and their applications in perovskite and other semiconductor-based optoelectronic devices," Light Sci. Appl. **10**, 174 (2021).

[19] S. Sundaram and E. Mazur, "Inducing and probing non-thermal transitions in semiconductors using femtosecond laser pulses." Nat. Mater. **1**, 217–224 (2002).

[20] G. Grancini, M. Maiuri, D. Fazzi, A. Petrozza, H.-J. Egelhaaf, D. Brida, G. Cerullo, and G. Lanzani, "Hot exciton dissociation in polymer solar cells," Nat. Mater. **12**, 29–33 (2013).

[21] A. E. Jailaubekov, A. P. Willard, J. R. Tritsch, W.-L. Chan, N. Sai, R. Gearba, L. G. Kaake, K. J. Williams, K. Leung, P. J. Rossky, and X.-Y. Zhu, "Hot charge-transfer excitons set the time limit for charge separation at donor/acceptor interfaces in organic

photovoltaics," Nat. Mater. **12**, 66–73 (2013).

[22] B. Hejda and K. Kral, "Hot-electron cooling and second-generation phonons in polar semiconductors," Phys. Rev. B **47**, 15554–15561 (1993).

[23] H. Zhu, K. Miyata, Y. Fu, J. Wang, P. P. Joshi, D. Niesner, K. W. Williams, S. Jin, and X.-Y. Zhu, "Screening in crystalline liquids protects energetic carriers in hybrid perovskites," Science **353**, 1409–1413 (2016).

[24] Y. Lan, B. J. Dringoli, D. A. Valverde-Chávez, C. S. Ponsenca Jr., M. Sutton, Y. He, M. G. Kanatzidis and D. G. Cooke, "Ultrafast correlated charge and lattice motion in a hybrid metal halide perovskite," Sci. Adv. **5**, eaaw5558 (2019).

[25] C. Wehrenfennig, G. E. Eperon, M. B. Johnston, H. J. Snaith, and L. M. Herz, "High Charge Carrier Mobilities and Lifetimes in Organolead Trihalide Perovskites," Adv. Mater. **26**, 1584–1589 (2014).

[26] C. Wehrenfennig, M. Liu, H. J. Snaith, M. B. Johnston, and L. M. Herz, "Charge-carrier dynamics in vapour-deposited films of organolead halide perovskite $CH_3NH_3Pb_{3-x}Cl_x$," Energy Environ. Sci. **7**, 2269 (2014).

[27] R. L. Milot, G. E. Eperon, H. J. Snaith, M. B. Johnston and L. M. Herz, "Temperature-Dependent Charge-Carrier Dynamics in $CH_3NH_3PbI_3$ Perovskite Thin Films," Adv. Func. Mater. **25**, 6218–6227 (2015).

[28] W. Rehman, R. L. Milot, G. E. Eperon, C. Wehrenfennig, J. L. Boland, H. J. Snaith, M. B. Johnston and L. M. Herz, "Charge-Carrier Dynamics and Mobilities in Formamidinium Lead Mixed-Halide Perovksites," Adv. Mater. **27**, 7938 (2015).

[29] M. Karakus, S. A. Jensen, F. D'Angelo, D. Turchinovich, M. Bonn and E. Cánovas, "Phonon-Electron Scattering Limits Free Charge Mobility in Methylammonium Lead Iodide Perovskites," J. Phys. Chem. Lett. **6**, 4991–4996 (2015).

[30] L. Luo, L. Men, Z. Liu, Y. Mudryk, X. Zhao, Y. Yao, J. M. Park, R. Shinar, J. Shinar, K.-M. Ho, I. E. Perakis, J. Vela and J. Wang, "Ultrafast terahertz snapshots of excitonic Rydberg states and electronic coherence in an organometal halide perovskite," Nat. Commun. **8**, 15565 (2017).

[31] M. P. Erodici, P. J. Pierone, N. T. P. Hartonon, J. Hidalgo, B. Laim T. Buonassisi, J.-P. Correa-Baena and M.-J. Sher, “Enhanced charge carrier lifetime mobility as a result of Rb and Cs incorporation in a halide perovskite,” Appl. Phys. Lett. **118**, 063901 (2021).

[32] H. Zhang, E. Debroye, B. Vina-Bausa, D. Valli, S. Fu, W. Zheng, L. Di Virgilio, L. Gao, J. M. Frost, A. Walsh, J. Hofkens, H. I. Wang and M. Bonn, “Stable Mott Polaron State Limits the Charge Density in Lead Halide Perovskites,” ACS Energy Lett. **8**, 420–428 (2023).

[33] G. R. Yettapu, D. Talukdar, S. Sarkar, A. Swarnkar, A. Nag, P. Ghosh, and P. Mandal, “Terahertz Conductivity within Colloidal $CsPbBr_3$ Perovskite Nanocrystals: Remarkably High Carrier Mobilities and Large Diffusion Lengths,” Nano Lett. **16**, 4838–4848 (2016).

[34] S. Sarkar, V. K. Ravi, S. Banerjee, G. R. Yettapu, G. B. Markad, A. Nag, and P. Mandal, “Terahertz Spectroscopic Probe of Hot Electron and Hole Transfer from Colloidal $CsPbBr_3$ Perovskite Nanocrystals,” Nano Lett. **17**, 5402–5407 (2017).

[35] E. Cinquanta, D. Meggiolaro, S. G. Motti, M. Gandini, M. J. P. Alcocer, Q. A. Akkerman, C. Vozzi, L. Manna, F. De Angelis, A. Petrozza and S. Stagira, “Ultrafast THz Probe of Photoniduced Polarons in Lead-Halide Perovskites,” Phys. Rev. Lett. **122**, 166601 (2019).

[36] A. M. Ulatowski, M. D. Farrar, H. J. Snaith, M. B. Johnston and L. M. Herz, “Revealing Ultrafast Charge-Carrier Thermalization in Tin-Iodide Perovskites through Novel Pump-Push-Probe Terahertz Spectroscopy,” ACS Photon. **8**, 2509–2518 (2021).

[37] B. Guzelturk, R. A. Belisle, M. D. Smith, K. Bruening, R. Prasanna, Y. Yuan, V. Gopalan, C. J. Tassone, H. I. Karunadasa, M. D. McGehee and A. M. Lindenberg, “Terahertz Emission from Hybrid Perovskites Driven by Ultrafast Charge Separation and Strong Electron-Phonon Coupling,” Adv. Mater. **30**, 1704737 (2018).

[38] M. Frenzel, M. Cherasse, J. M. Urban, F. Wang, B. Xiang, L. Nest, L. Huber, L. Perfetti, M. Wolf, T. Kampfrash, X.-Y. Zhu, and S. F. Maehrlein, “Nonlinear terahertz control of the lead halide perovskite lattice,” Sci. Adv. **9**, eadg3856 (2023).

[39] Z. Yang, A. Surrente, K. Galkowski, A. Miyata, O. Portugall, R. J. Sutton, A. A.

Haghighirad, H. J. Snaith, D. K. Maude, P. Plochocka, and R. J. Nicholas, “Impact of the Halide Cage on the Electronic Properties of Fully Inorganic Cesium Lead Halide Perovskites,” ACS Energy Lett. **2**, 1621–1627 (2017).

[40] C. A. López, C. Abia, M. C. Alvarez-Galván, B.-K. Hong, M. V. Martínez-Huerta, F. Serrano-Sánchez, F. Carrascoso, A. Castellanos-Gómez, M. T. Fernández-Díaz, and J. A. Alonso, “Crystal Structure Features of $CsPbBr_3$ Perovskite Prepared by Mechanochemical Synthesis,” ACS Omega **5**, 5931–5938 (2020).

[41] F. H. Su, F. Blanchard, G. Sharma, L. Razzari, A. Ayesheshim, T. L. Cocker, L. V. Titova, T. Ozaki, J.-C. Kieffer, R. Morandotti, M. Reid and F. A. Hegmann, “Terahertz pulse induced intervalley scattering in photoexcited GaAs,” Opt. Express **17**, 9620 (2009).

[42] F. Blanchard, D. Golde, F. H. Su, L. Razzari, G. Sharma, R. Morandotti, T. Ozaki, M. Reid, M. Kira, S. W. Koch and F. A. Hegmann, “Effective Mass Anisotropy of Hot Electrons in Nonparabolic Conduction Bands of *n*-Doped InGaAs Films Using Ultrafast Terahertz Pump-Probe Techniques,” Phys. Rev. Lett. **107**, 107401 (2011).

[43] P. Yadav, K. Moon, A. Biswas, C. K. Herrera, Y. Zhang, S. C. Barton, R. R. Lunt, G. J. Blanchard, and S. Kim, “Morphology-Controlled Vapor-Phase Nanowire Growth with Ruddlesden-Popper Lead Bromide Perovskite,” Chem. Mater. **35**, 3300–3306 (2023).

[44] N. V. Smith, “Classical generalization of the Drude formula for the optical conductivity,” Phys. Rev. B **64**, 155106 (2001).

[45] H. Nemec, P. Kuzel and V. Sundström, “Far-infrared response of free charge carriers localized in semiconductor nanoparticles,” Phys. Rev. B **79**, 115309 (2009).

[46] T. L. Cocker, D. Baillie, M. Buruma, L. V. Titova, R. D. Sydora, F. Marsiglio and F. A. Hegmann, “Microscopic origin of the Drude-Smith model,” Phys. Rev. B **96**, 205439 (2017).

[47] L. Protesescu, S. Yakunin, M. I. Bodnarchuk, F. Krieg, R. Caputo, C. H. Hendon, R. X. Yang, A. Walsh, and M. V. Kovalenko, “Nanocrystals of Cesium Lead Halide Perovskites ($CsPbX_3$, X = Cl, Br, and I): Novel Optoelectronic Materials Showing Bright

Emission with Wide Color Gamut," Nano Lett. **15**, 3692–3696 (2015).

[48] B. Ai, C. Liu, Z. Deng, J. Wang, J. Han, and X. Zhao, "Low temperature photoluminescence properties of $CsPbBr_3$ quantum dots embedded in glasses," Phys. Chem. Chem. Phys. **19**, 17349 (2017).

[49] J. Ramade, L. M. Andriambariarijaona, V. Steinmetz, N. Goubet, L. Legrand, T. Barisien, F. Bernardot, C. Testelin, E. Lhuillier, A. Bramati, and M. Chamarro, "Fine structure of excitons and electron-hole exchange energy in polymorphic $CsPbBr_3$ single nanocrystals," Nanoscale **10**, 6393–6401 (2018).

[50] Y. Liu, J. Wang, L. Zhang, W. Lium C. Wu, C. Liu, Z. Wu, L. Xiao, Z. Chen, and S. Wang, "Exciton and bi-exciton mechanisms in amplified spontaneous emission from $CsPbBr_3$ perovskite thin films," Opt. Express **27**, 29125 (2019).

[51] W. Du, S. Zhang, Z. Wu, Q. Shang, Y. Mi, J. Chen, C. Qin, X. Qiu, Q. Zhang, and X. Lu, "Unveiling lasing mechanism in $CsPbBr_3$ microsphere cavities," Nanoscale **11**, 3145 (2019).

[52] X. Shen, M. Chen, L. Shi, F. Chen, Y. Liu, D. Cao, and C. Xu, "Lasing behaviors in solution processed all-inorganic $CsPbBr_3$ perovskite microsized crystals," Opt. Commun. **453**, 124354 (2019).

[53] L. Zhang, X. Li, Y. Song, and B. Zou, "Ultrafast Antisolvent Growth of Single-Crystal $CsPbBr_3$ Microcavity for Whispering-Gallery-Mode Lasing," Nanomaterials **13**, 2116 (2023).

[54] C. L. Davies, M. R. Filip, J. B. Patel, T. W. Crothers, C. Verdi, A. D. Wright, R. L. Milot, F. Giustino, M. B. Johnston, and L. M. Herz, "Bimolecular recombination in methylammonium lead triiodide perovskite is an inverse absorption process," Nat. Commun. **9**, 293 (2018).

[55] R. Kaindl, M. A. Carnahan, D. Hägele, R. Lövenich, and D. S. Chemla, "Ultrafast terahertz probes of transient conducting and insulating phases in an electron-hole gas," Nature **423**, 734–738 (2003).

[56] C. Poellmann, P. Steinleitner, U. Leierseder, P. Nagler, G. Plechinger, M. Porer, R.

Bratschitsch, C. Schüller, T. Korn, and R. Huber, “Resonant internal quantum transitions and femtosecond radiative decay of excitons in monolayer WSe_2,” Nat. Mater. **14**, 889–893 (2015).

[57] Y. Kang and S. Han, “Intrinsic Carrier Mobility of Cesium Lead Halide Perovskites,” Phys. Rev. Appl. **10**, 044013 (2018).

[58] X. Chen, Y. Wang, J. Song, X. Li, J. Xu, H. Zeng, and H. Sun, “Temperature Dependent Reflectance and Ellipsometry Studies on a $CsPbBr_3$ Single Crystal,” J. Phys. Chem. C **123**, 10564 (2019).

[59] A. Burgos-Caminal, E. Socie, M. E. F. Bouduban, and J.-E. Moser, “Exciton and Carrier Dynamics in Two-Dimensional Perovskites,” J. Phys. Chem. Lett. **11**, 7692–7701 (2020).

[60] S. G. Motti, M. Kober-Czerny, M. Righetto, P. Holzhey, J. Smith, H. Kraus, H. J. Snaith, M. B. Johnston, and L. M. Herz, “Exciton Formation Dynamics and Band-Like Free Charge-Carrier Transport in 2D Metal Halide Perovskite Semiconductors,” Adv. Func. Mater. **33**, 2300263 (2023).

[61] F. H. Balogun, N. P. Gallop, D. Sirbu, J. D. Hutchinson, N. Hill, J. M. Woolley, D. Walker, S. York, P. Docampo, and R. L. Milot, “Untangling free carrier and exciton dynamics in layered hybrid perovskites using ultrafast optical and terahertz spectroscopy,” Mater. Res. Express **11**, 025503 (2024).

[62] L. B. Tan, O. Cotlet, A. Bergschneider, R. Schmidt, P. Back, Y. Shimazaki, M. Kroner, and Imamoglu, “Interacting Polaron-Polaritons,” Phys. Rev. X **10**, 021011 (2020).

[63] J. B. Muir, J. Levinsen, S. K. Earl, M. A. Conway, J. H. Cole, M. Wurdack, R. Mishra, D. J. Ing, E. Estrecho, Y. Lu, D. K. Efimkin, J. O. Tollerud, E. A. Ostrovskaya, M. M. Parish, and J. A. Davis, “Interactions between Fermi polarons in monolayer WS_2,” Nat. Commun. **13**, 6164 (2022).

[64] P. U. Jepsen, D. G. Cooke, and M. Koch, “Terahertz spectroscopy and imaging – Modern techniques and applications,” Laser Photon. Rev. **5**, 124–166 (2011).